Filterless narrowband photodetectors enabled by controllable band modulation through ion migration: the case of halide perovskites

Yu Li, Shanshan Yu, Junjie Yang, Kai Zhang, Mingyu Hu, Weitao Qiu, Fumin Guo, Wei Qian, Sean Reinecke, Tao Chen, Makhsud I. Saidaminov, Jian Wang & Shihe Yang

2023

Original citation:

Li, Y., Yu, S., Yang, J., Zhang, K., Hu, M., Qiu, W., Guo, F., Qian, W., Reinecke, S., Chen, T., Saidaminov, M. I., Wang, J., & Yang, S. (2023). Filterless narrowband photodetectors enabled by controllable band modulation through ion migration: the case of halide perovskites. *InfoMat, 6*(1). https://doi.org/10.1002/inf2.12506

Received: 28 July 2023 | Revised: 23 October 2023 | Accepted: 9 November 2023

DOI: 10.1002/inf2.12506

RESEARCH ARTICLE

WILEY

Filterless narrowband photodetectors enabled by controllable band modulation through ion migration: The case of halide perovskites

Yu Li[1,2,3] | Shanshan Yu[1,2,3,4] | Junjie Yang[5] | Kai Zhang[1,2,3] | Mingyu Hu[1] | Weitao Qiu[1] | Fumin Guo[1,6] | Wei Qian[1,3] | Sean Reinecke[7] | Tao Chen[4] | Makhsud I. Saidaminov[7] | Jian Wang[1,2,3] | Shihe Yang[1,2,3]

[1]Guangdong Provincial Key Lab of Nano-Micro Materials Research, School of Chemical Biology and Biotechnology, Shenzhen Graduate School, Peking University, Shenzhen, Guangdong, the People's Republic of China

[2]Shenzhen Bay Laboratory, Institute of Biomedical Engineering, Shenzhen, Guangdong, the People's Republic of China

[3]School of Advanced Materials, Shenzhen Graduate School, Peking University, Shenzhen, Guangdong, the People's Republic of China

[4]Department of Chemistry, The University of Hong Kong, Hong Kong SAR, the People's Republic of China

[5]Hefei National Laboratory for Physical Sciences at Microscale, CAS Key Laboratory of Materials for Energy Conversion, Department of Materials Science and Engineering, School of Chemistry and Materials Science, University of Science and Technology of China, Hefei, Anhui, the People's Republic of China

[6]College of Materials and Energy, South China Agricultural University, Guangzhou, Guangdong, the People's Republic of China

[7]Department of Chemistry, University of Victoria, Victoria, British Columbia, Canada

Correspondence

Jian Wang and Shihe Yang, Guangdong Provincial Key Lab of Nano-Micro Materials Research, School of Chemical Biology and Biotechnology, Shenzhen Graduate School, Peking University, Shenzhen, Guangdong 518055, the People's Republic of China.

Email: jianwsolar@pku.edu.cn and chsyang@pku.edu.cn

Funding information

National Natural Science Foundation of China, Grant/Award Numbers: 21972006, 22275180, U2001217, 22261160370, 52202182; Shenzhen Peacock plan, Grant/Award Number: KQTD2016053015544057; Shenzhen Innovation Fund, Grant/Award Number: JCYJ20220818101018038; Natural Sciences and Engineering Research Council of Canada, Grant/Award Number: RGPIN-2020-04239

Abstract

Narrowband photodetectors conventionally rely on optical structure design or bandpass filters to achieve the narrowband regime. Recently, a strategy for filterless narrowband photoresponse based on the charge collection narrowing (CCN) mechanism was reported. However, the CCN strategy requires an electrically and optically "thick" photoactive layer, which poses challenges in controlling the narrowband photoresponse. Here we propose a novel strategy for constructing narrowband photodetectors by leveraging the inherent ion migration in perovskites, which we term "band modulation narrowing" (BMN). By manipulating the ion migration with external stimuli such as illumination, temperature, and bias voltage, we can regulate in situ the energy-band structure of perovskite photodetectors (PPDs) and hence their spectral response. Combining the Fermi energy levels obtained by the Kelvin probe force microscopy, the internal potential profiles from solar cell capacitance simulator simulation, and the anion accumulation revealed by the transient ion-drift technique, we discover two critical mechanisms behind our BMN strategy: the extension of an optically active but electronically dead region proximal to the

---

Yu Li, Shanshan Yu, and Junjie Yang contributed equally to this work.

top electrode and the down-bending energy bands near the electron transport layer. Our findings offer a case for harnessing the often-annoying ion migration for developing advanced narrowband PPDs.

KEYWORDS
band structure, ion migration, narrowband detection, perovskite, spatial distribution of charge carriers

1 | INTRODUCTION

Narrowband photodetectors with high selectivity to a specific wavelength play a crucial role in applications such as multi-color imaging, machine vision, biomedical imaging, and optical communications. Various strategies have been developed to achieve narrowband photodetection, including filtering methods[1–4] that utilize optical bandpass filters in combination with broadband photodetectors, and nonfiltering methods such as exclusive absorption in the target spectral range determined by their intrinsic properties,[5,6] the plasmonic effect,[7] or charge collection narrowing (CCN) effect.[4,8–11] Although commercial narrowband photodetectors based on the filtering methods offer narrow full width at half maximum (FWHM) responsivity, they suffer from complex photodetector structures, high fabrication costs, high energy losses, incompatibility with device miniaturization, limited optical resolution, and color inconsistency.[12]

Significant attention has recently been paid to the CCN mechanism in perovskite-based photodetectors (PPDs). This approach utilizes surface defect states to trigger the Shockley–Read–Hall recombination of charge carriers generated by short-wavelength photons. A thick photoactive layer spatially separates the surface "recombination region" with a high absorption coefficient (α) and the bulk "photogeneration region" with a low-α.[8] To improve the narrowband response of PPDs, researchers have made efforts to quench short-wavelength generated photocarriers by introducing photoactive materials with high trap density at the front contact side via doping or structure design, such as 2D perovskites with multi-quantum well structures or organic macromolecules.[10,13] However, recombination losses caused by high-density defects impact not only the short-wavelength response but also the target long-wavelength response. Furthermore, the requirement for an electrically and optically "thick" perovskite photoactive layer presents an additional challenge. Precise control over trap states in the active layer to achieve the desired narrowband response remains elusive.

Here we report a new mechanism for narrowband photodetection, termed band modulation narrowing (BMN), by utilizing ion migration to deliberately manipulate the energy band structure of PPDs and hence their spectral response. Applying external stimuli, such as illumination, temperature, and bias voltage, we can control the ion migration profile in the PPDs, forming a flat energy band with an optically active but electronically dead (OAED) region proximal to the incident electrode and the down-bending energy band adjacent to the electron transport layer. We then show that the energy-band diagram, photon absorption bandwidth, and charge collection in the device can be spatially adjusted to achieve the desired narrowband photoresponse. The BMN strategy offers efficient control over the response characteristics and performance of PPDs by reconfiguring the OAED region and energy band structure within the device.

2 | FABRICATION AND CHARACTERIZATION OF SELF-FILTERLESS NARROWBAND PPDs

Halide perovskites are known to exhibit ion migration under voltage bias[14,15] or light irradiation[16,17] due to their low activation energy (E_a). Ion migration is generally considered detrimental to perovskite-based photoelectric devices such as solar cells, as it leads to hysteresis,[18,19] open-circuit voltage decay,[20] and performance degradation.[21,22] On the other hand, this process was also reported to be responsible for healing solar cells through the "light soaking effect"[23,24] and for fast switching of memory devices.[24,25] Ion migration reconfigures the ion distribution and internal potential profile and hence influences the optical absorption and carrier-generation characteristics of devices.[24,26–28] The absorption depth of photons depends on the absorption cross-section, α, (known as Beer–Lambert law); the latter, on its own, varies for different wavelengths. We posited that ion accumulation at the interface creates an electric field in the PPDs, leading to band modulation and an asymmetric distribution of space charges generated by short-wavelength and long-wavelength photons. Consequently, coupling the spatial distribution of photon absorption and the band structure is expected to manipulate charge collection and separation efficiencies, as well as the response window of PPDs; this is the central focus and objective of this work and will be demonstrated in the subsequent sections.

The perovskite films were fabricated by a home-built aerosol–liquid–solid (ALS) deposition method,[9,29–31] which can control the thickness of the perovskite film from nanometer to micrometer scale by varying the number of deposition cycles; and fabricate films with varying compositions by adjusting the chemistry of feed solution. The top-view scanning electron microscopy (SEM) image of ALS-deposited $MAPbI_3$ (MA = methylammonium) perovskite film shows a smooth surface and large grain sizes (Figure 1A and Figure S1). The x-ray diffraction (XRD) pattern shows peaks at 2θ values of 14.2°, 20.1°, 28.6°, 31.6°, and 32.0°, corresponding to the (110), (200), (220), (114), and (310) planes of the tetragonal structure of $MAPbI_3$ (Figure S2). Notably, the (110) diffraction peaks are dominant in the perovskite thick films, demonstrating a preferential growth along the <110> crystallographic direction.[32,33] The corresponding transmittance spectrum and photoluminescence spectrum are presented in Figure 1C. The asymmetric and red-shift photoluminescence spectrum is caused by the photon recycling effect in the thick perovskite film.[9,34]

The as-prepared perovskite films were then used to construct the p–i–n type PPDs in FTO/NiO_x/perovskite/PCBM/PPDIN6/Ag architecture, where PCBM is phenyl-C61-butyric acid methyl ester and PPDIN6 is amino-functionalized perylene diimide polymer (Figure 1D). A thin PPDIN6 layer was used to modulate the cathode interface and inhibit the inward diffusion of Ag^+ and outward diffusion of I^- toward the top Ag electrode.[35] The perovskite film was ∼25 μm thick as shown in Figure S3. The device operates without external bias unless otherwise noted. Figure 1E presents the EQE spectra of the fabricated PPDs before and after illumination. The PPD after illumination exhibits a dominant narrow peak at 790 nm with FWHM less than 16 nm, which is in strong contrast to the typical broadband response observed before illumination treatment. Specifically, the PPDs after light illumination suffered a tremendous EQE loss from 300 to 770 nm but maintained ∼60% of the reference device EQE value at 790 nm, resulting in a wavelength selective narrowband photoresponse with a peak EQE of ∼21%. After the device was stored in the dark for over 2 h, the

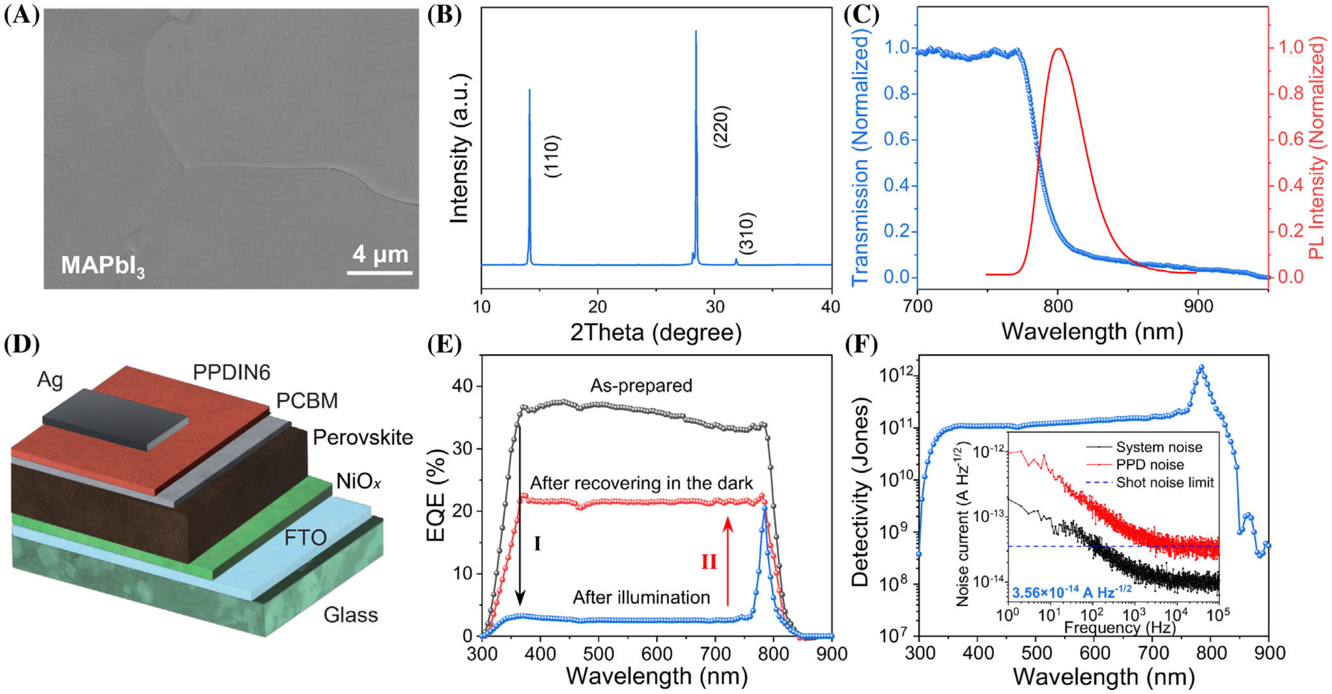

FIGURE 1 Fabrication and characterization of filterless narrowband PPDs. (A) Top-view SEM image of $MAPbI_3$ perovskite film fabricated by ALS method. (B) XRD pattern of $MAPbI_3$ perovskite film. (C) Normalized transmittance spectrum (dotted lines) and photoluminescence spectrum (solid lines) of $MAPbI_3$ perovskite film. (D) Device architecture of the p-i-n type self-filtering narrowband PPD with NiO_x/PCBM, PPDIN6, and Ag acting as the hole/electron transport layers (HTL/ETL), interfacial layer, and counter electrode, respectively. (E) EQE spectra of the as-fabricated pristine $MAPbI_3$-based PPD, the device tested after illumination for 10 min, and the device tested after recovering in the dark for 2 h. (F) Specific detectivity of $MAPbI_3$-based self-filtering narrowband PPD. Inset: Noise spectrum of the PPD and the system noise of the noise meter.

responses from the short-wavelength region were restored albeit not exactly to the original level. We also fabricated the PPDs based on other perovskite materials (Figures S4, S5), including hybrid perovskites (such as $MAPbCl_3$, $MAPbBr_3$, $MAPbI_xBr_{3-x}$, $MAPbBr_xCl_{3-x}$, $FA_xMA_{1-x}PbI_3$) and all-inorganic perovskites (such as $CsPbBr_3$, $CsPbI_xBr_{3-x}$). All these devices presented a controllable photoresponse (Figure S5), since ion migration is inherent to halide perovskite materials. Our other related work[36] based on this strategy was focused on the intentional introduction of excess ions into the perovskite to increase the mobile ion concentration and thus to reduce the ion migration barrier (Figure S5D).

We then measured the PPDs' current–voltage (I–V) characteristics, specific detectivity, response speed, and stability. The asymmetric behavior of the I–V curves in the dark and under illumination at 790 nm indicates high rectification characteristics and the formation of a photodiode structure (Figure S6). The shift in the minima of the dark I–V response is due to ion migration and accumulation at the interfaces under bias.[37,38] The total noise currents (i_n) were obtained from a fast Fourier transform of dark current as a function of time at 0 V bias. The specific detectivity (D^*) can be calculated from the noise equivalent power (NEP) according to

$$\mathrm{NEP} = \frac{i_n}{R} \tag{1}$$

$$D^* = \frac{\sqrt{A\Delta f}}{\mathrm{NEP}} \tag{2}$$

where A is the active area of the photodetector and $\triangle f$ is the bandwidth.

As displayed in Figure 1F, flicker noise ($1/f$) dominates the noise current in the low-frequency range. The total noise current of PPD approaches the shot noise limit (3.56×10^{-14} A Hz$^{-1/2}$) and becomes frequency-independent in the high-frequency range. The NEP of the PPD at 790 nm was calculated to be 2.74×10^{-13} W Hz$^{-1/2}$ at a modulation frequency of 4 kHz. The D^* reaches the maximum of 1.46×10^{12} Jones (cm Hz$^{1/2}$ W^{-1}) as shown in Figure 1F. We then estimated the linear dynamic range (LDR) which can describe the response range of the varied incident light intensities (Figure S7):

$$\mathrm{LDR} = 20 \log \frac{J_{\max}}{J_{\min}} \tag{3}$$

where $J_{\max}$ and $J_{\min}$ are the maximum and minimum of the photocurrent density in the region of linear photosensitivity.

The $J_{\max}$ and $J_{\min}$ were measured to be 6.85×10^{-5} and 1.71×10^{-9} A cm^{-2}, respectively. The LDR of the p-i-n type PPD based on $MAPbI_3$ exhibited a value of 92 dB in the light density range from 0.549 W cm^{-2} to 4.53 μW cm^{-2}. The linear relationship of photocurrent versus light intensity manifests the ability of the PPDs to detect light across a large intensity range. The rising and falling time of the narrowband PPDs, that is, the time for the photocurrent to increase from 10% to 90% of the peak value and decrease from 90% to 10% of the peak value, were estimated to be 2.71 and 3.41 ms, respectively (Figure S8). The PPDs without encapsulation in ambient air with a relative humidity of ~60% present excellent stability after over 5000 ON/OFF cycles under illumination at 790 nm (Figure S9). In addition, 84% of the initial photocurrent of the device is maintained after storage in an N_2-filled glove box for 2 weeks (Figures S10A,B). These results demonstrate the excellent optoelectrical properties and stability of the narrowband PPDs based on our proposed BMN strategy.

3 | MECHANISM OF THE BMN-ENABLED SELF-FILTERING NARROWBAND PHOTODETECTION

When no ion migration is present, the devices are expected to have a uniform built-in electric field (E_{bi}) in the perovskite layer, pointing from the n-PCBM layer to the p-NiO_x layer at 0 V bias (Figure 2A).[39–41] Due to linear potential drop, electrons and holes excited by photons at various wavelengths can be extracted through the ETL (PCBM) and HTL (NiO_x), resulting in a broadband EQE response (Figure 1E).[42] However, for the PPDs, ions drift under E_{bi} across the perovskite layer and accumulate at the interfaces (Figure 2D). This creates an ion-induced electric field (E_{ion}) opposing E_{bi}. The E_{ion} can cause an ionic shielding effect[20,43] and changes the band structure (Figure 2D). As a consequence, in the perovskite layer in the vicinity of the p-NiO_x, the net electric field distribution ($E_{net} = E_{bi} - E_{ion}$) is reduced, extending the OAED region, which is critical for reducing the photoresponse in the short-wavelength region due to the limited diffusion length of charge carriers. Simultaneously, the E_{net} intensifies the band bending near the n-PCBM (Figure 2D), enabling efficient extraction of charge carriers generated by the long-wavelength photons.

To test our hypothesis, we studied our devices by the peak force Kelvin probe force microscopy (KPFM). The thickness of the perovskite layer in the PPD is ~4.7 μm (Figure S11). The measurement was conducted under open-circuit conditions in the dark for the as-fabricated PPD without illumination (Figures 2B,C) and for the device after

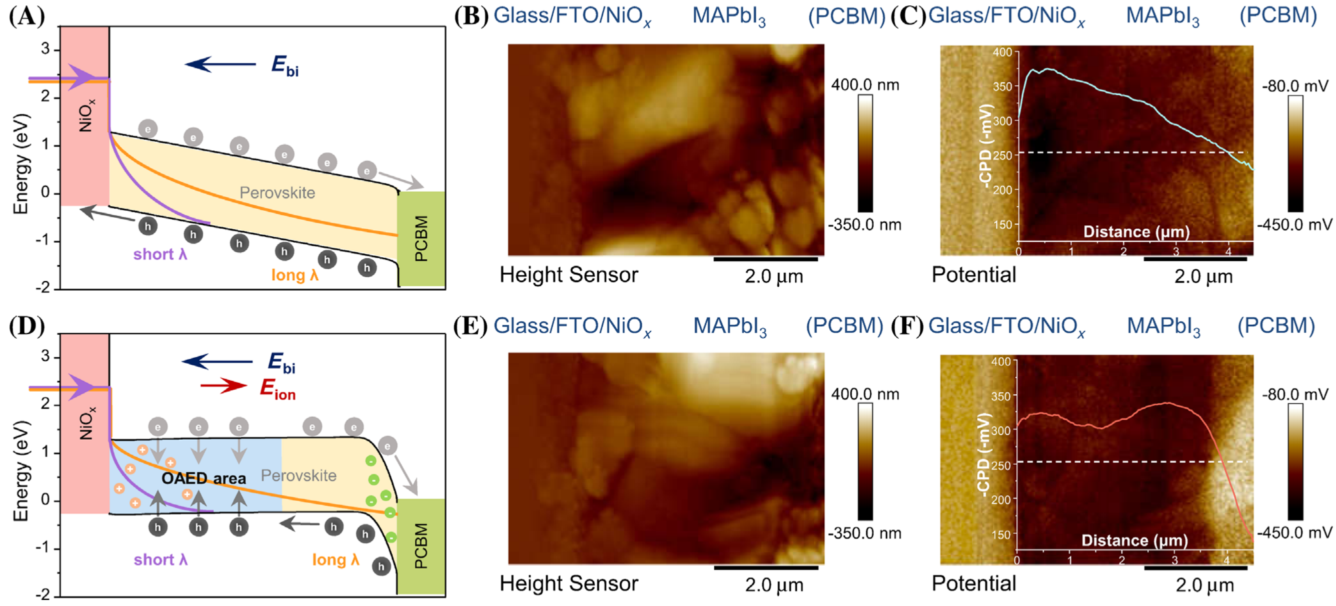

FIGURE 2 Mechanism of BMN-enabled narrowband PPDs. (A,D) Band structure schematic showing the charge separation/collection of p-i-n type photodetectors under short-wavelength and long-wavelength illumination before (A) and after (D) ion migration. (B,C,E,F) Scanning probe microscopic images of as-fabricated narrowband PPDs before and after illumination. Height (B) and potential images (C) of the fresh PPD's cross-section before illumination, and the corresponding (−CPD) line profiles from FTO to perovskite layer (C). Height (E) and potential images (F) of the PPD's cross-section after illumination treatment, and the corresponding (−CPD) line profiles from FTO to perovskite layer (F).

illumination for 10 min (then test at once) (Figures 2E,F). The work functions of PPDs (Φ_{PPD}) are determined by the contact potential difference (CPD) between the Pt/Ir-coated conductive cantilever probe and PPDs:

$$\emptyset_{\text{PPD}} = \emptyset_{\text{probe}} + q \times \text{CPD} \tag{4}$$

where q is the elementary charge.

Equation (4) shows that the work functions are linearly correlated with the obtained CPD values of the PPD. The −CPD trends in the direction from FTO to the perovskite layer are shown in Figures 2C,F which represent the corresponding vacuum level profiles. In the dark, the device exhibits a continuous potential difference of ~0.15 V (from 0.375 to 0.225 V) across the perovskite layer from the FTO side to the n-PCBM side (Figure 2C). However, after illumination, the work function of the PPD displays a small fluctuation across the perovskite layer from the FTO side, while the Fermi energy of the perovskite near the n-PCBM side falls sharply by ~0.19 V (from 0.325 to 0.135 V) (Figure 2F). We can thus conclude that the observed illumination-induced narrowband photoresponse is attributed to the extension of the OAED region near the p-NiO$_x$ side which limits the carrier diffusion length, while the down-bending energy band close to the n-PCBM side enhances electron collection.

4 | DISCUSSION

We further delve into the influence of ion migration on the above two critical factors, and thus on the filterless narrowband photoresponse of the p-i-n type PPDs. The following questions should be addressed:

i. Which ions play a dominant role in the ion redistribution process and subsequently induce the energy-band changes in the BMN-enabled self-filtering narrowband PPDs?
ii. How does ion migration affect the OAED layer and further shape the EQE response of the PPDs?

4.1 | Detection of ion migration in the BMN-enabled self-filtering narrowband PPDs

Both anions and cations can migrate in perovskites, especially in the presence of defects such as vacancies, interstitials, or antisite substitutions. To address the first question above, we employed the transient ion-drift (TID),[44,45] which can provide qualitative pictures of ion migration along with the nature of migrating ion species, ion-migration activation energy (E_a), migrating ion concentration (N_{ion}) and ion diffusion coefficient (D_{ion})

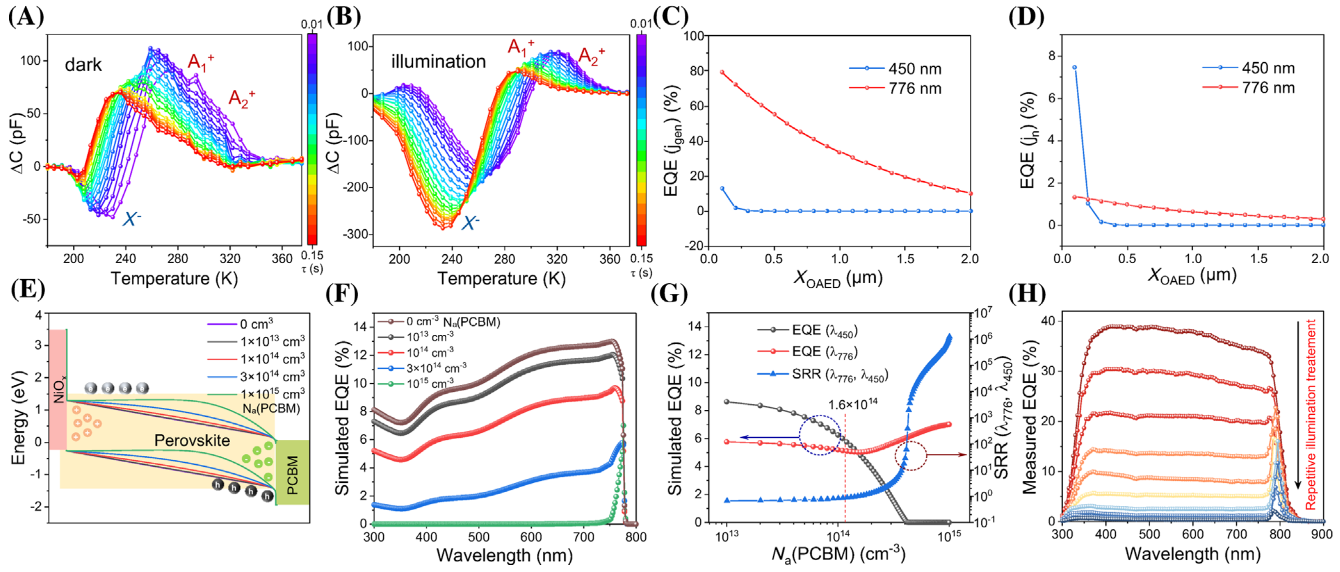

FIGURE 3 The dependence of photoresponse of BMN-enabled self-filtering narrowband PPDs on the OAED layer affected by ion migration. (A,B) Rate-window plots of capacitance transients of $MAPbI_3$ PPDs from the transient ion drift (TID) measurements in the dark (A) and under the illumination of a 635 nm laser (B). The different time constants ranging in color gradation reveal three ion species with different time constants. The negative peak (X^-) is assigned to the migration of interstitial I^- and the two positive peaks (A_1^+, A_2^+) to the migration of MA^+. (C,D) Simulated EQE versus x_{OAED} at the short-wavelength (450 nm) and the absorption edge (776 nm) contributed by j_{gen} (C) and by j_n (D). (E–G) SCAPS device simulation of p-i-n type photodetector with and without ion migration-coupled drift-diffusion: Simulated results: (E) Energy band diagram of the $MAPbI_3$ PPDs with different N_a(PCBM); (F) EQE spectra of the $MAPbI_3$ PPDs at different N_a(PCBM); (G) Plots of EQE and SRR versus N_a(PCBM) at the wavelengths of 450 and 776 nm (G). In these simulations, the acceptor density was set to increase linearly from the p-NiO_x side ($N_a(NiO_x) = 0$) to the n-PCBM side (N_a(PCBM)). (H) Ten experimental EQE curves of the $MAPbI_3$ PPDs measured successively, with each undergoing illumination treatment.

(Figures 3A,B). To start the measurement, a voltage bias was applied on the device to collapse the depletion layer completely, causing the mobile ions to diffuse uniformly within the collapsed depleted region. Subsequently, by removing the bias, the mobile ions will drift back to the contact interfaces under the inherent E_{bi}, thereby restoring the original depletion width. During this drifting process, characteristic signals of the capacitance transients are tracked at different temperatures to reveal the ion migration. To avoid interference from ion migration behavior outside the perovskite layer, we opted for the inverted perovskite solar cell structure based on the architecture of FTO/NiO_x/perovskite/PCBM/$PPDIN_6$/Ag instead of the conventional one. As a first-order approximation, the capacitance transients in our PPDs can approximately reflect the ion migration characteristics inside the perovskite layer[46,47] due to the inhibited dipoles at the NiO_x/perovskite interface by the diethanolamine (DEA),[48,49] and the negligible interfacial defects after passivation by the PCBM and PPDIN6.[35,50,51]

Given that both defect states (the trap states within the bandgap that can capture and emit electrons/holes) and ion migration (drift and diffusion of mobile ions) can contribute to the capacitance transients, we first compared the decay and rise time of capacitance for the capture/diffusion (τ_1) and emission/drift (τ_2) processes of the PPDs (Figures S12A,B). The decay time required to form a uniform ion distribution after applying a forward bias (1 V) on the PPDs is much longer than the rise time required for the ions to drift back to the interfaces after removing the forward bias under both dark and illumination conditions ($\tau_1 >> \tau_2$), confirming the ion-migration origin of the capacitance transients. Otherwise, the capture process would be faster than the thermally activated emission process ($\tau_1 << \tau_2$).[45] In light of this consideration, we first applied a forward bias of 1 V close to the E_{bi} of the devices (0.819 eV, Figure S13) for 1 s to fully deplete the perovskite devices and redistribute the ions, either in the dark or under illumination. Then the capacitance transients after removing the bias were recorded (Figures S14A,B). The TID capacitance transients were fitted to the following Equations (5–7) to find the best global fit values for $\Delta C_n(T)$ and τ_n (see Text S1 for details) and to finally obtain the E_a, N_{ion}, and D_{ion}.

$$C(t,T) = C_\infty(T) + \sum_n \Delta C_n(T) \exp\left\{\frac{-t}{\tau_n}\right\} \tag{5}$$

$$\tau_n = \frac{k_B T \varepsilon_0 \varepsilon_r}{q^2 D_{ion} N_D} \tag{6}$$

$$D_{\mathrm{ion}} = D_0 \exp\left(-\frac{E_a}{k_B T}\right) \tag{7}$$

In these equations, $C(t, T)$ is the capacitance as a function of time and temperature, $C_\infty(T)$ is the steady-state capacitance, which can be extracted directly from measurements at a temperature of T, $\Delta C_n(T)$ is the capacitance magnitude at temperature T of the ion migration process n, D_0, and τ_n are the exponential prefactor and time constant of the process n, respectively, k_B is the Boltzmann constant, ε_r is the perovskite relative permittivity, ε_0 is the vacuum permittivity, and N_D is the doping density. Every ion migration pathway can be fitted with one to three capacitance decay/rise traces under dark and illumination conditions. Each of the exponential terms in equation (5) represents one specific ion migration process n.

By choosing $t_1 = 5t_2$, the capacitance change trends were extracted from Figures S14A,B as $\triangle C = C(t_2) - C(t_1)$ in a rate-window plot. The capacitance changes can be assigned to the migration of cations (positive trends, that is, $\triangle C > 0$) or anions (negative trends, that is, $\triangle C < 0$) in a p-type semiconductor,[44,45,52] as shown in Figures 3A,B. The E_a parameters were extracted from the slopes of the Arrhenius plots according to Equation (7), as shown in Figures S14C,D. Therefore, we assigned the negative peak (X^-) to the migration of interstitial I^- with an E_a of 0.423 eV and the two positive peaks (A_1^+, A_2^+) to the migration of MA^+ ($E_a = 0.597$, 0.570 eV) instead of H^+ (with a too low E_a of 0.29 eV)[53] and Pb^{2+} (with a too high E_a of 2.31 eV).[47] According to Futscher et al,[45] the A_1^+ and A_2^+ entail two different migration pathways of MA^+ associated with the volume change in the unit cell at the temperatures close to the tetragonal-cubic phase transition. This agrees with computationally predicted E_a of I^- (between 0.08 and 0.6 eV),[26,54] which is generally lower than that of MA^+ (between 0.46 and 1.12 eV).[54,55]

As summarized in Table S1, the concentration of mobile MA^+ ions (7.05×10^{14} cm^{-3} for A_1^+ and 4.77×10^{13} cm^{-3} for A_2^+) are much higher than that of the mobile I^- ions (4.16×10^{13} cm^{-3}) in the dark (Figures 3A and Figure S14C). Compared to I^-, however, the relatively high activation energies of 0.597 (A_1^+) and 0.570 eV (A_2^+) results in a lower migration rate for MA^+ ions. Indeed, the ion diffusion coefficient (D_{ion}) we obtained for I^- at 300 K (3.65×10^{-8} cm^2 s^{-1}) is one or two orders of magnitude higher than that for MA^+ ions (5.98×10^{-9} and 3.92×10^{-10} cm^2 s^{-1} for A_1^+ and A_2^+, respectively), in agreement with the previous reports.[45,46,56–58] It is noteworthy that the illumination has significantly changed the situation. Specifically, for the $MAPbI_3$-based PPDs under illumination, as shown in Figure 3B and Figure S14D, we observe a larger negative peak (I^-) than the positive peaks (A_1^+, A_2^+) together with the decreased E_a for all ions (0.529 and 0.462 eV for MA^+, 0.314 eV for I^-). The higher N_{ion} and decreased E_a for all the ions under illumination attest to the enhanced ion migration for PPDs. Notably, the concentration of mobile I^- ions under illumination (1.21×10^{15} cm^{-3}) is 29 times that of mobile I^- ions in the dark (4.16×10^{13} cm^{-3}). Meanwhile, N_{ion} for the MA^+ was increased to 8.05×10^{14} cm^{-3} for A_1^+ (substantial increase) and 2.74×10^{14} cm^{-3} for A_2^+ (fivefold increase) under continuous illumination at 635 nm. For the D_{ion} under laser illumination, we obtained slightly reduced D_{ion} for A_1^+ (1.16×10^{-9} cm^2 s^{-1}) and I^- (1.86×10^{-8} cm^2 s^{-1}) but slightly increased D_{ion} for A_2^+ (4.83×10^{-10} cm^2 s^{-1}). Under the illumination, one might expect an increased D_{ion} caused by the reduced E_a, but the reduced entropy gain during the ion migration toward the interfaces counterbalances this effect.[59] Thus, the resulting change in D_{ion} is complex and calls for further investigations.

We can thus conclude that the accumulation of anions at the perovskite/PCBM interface in p-i-n-type PPDs plays a decisive role than the accumulation of cations at the NiO_x/perovskite interface in the band modulation and narrowband response. To challenge our conclusion, we also fabricated n-i-p type PPDs with the structure of FTO/TiO_2/perovskite/PTAA/Ag (PTAA = *poly*-triarylamine). As we expected, the narrowband response was not observed after continuous illumination for the accumulation of anions at the TiO_2/perovskite interface (Figure S15). The dominant migration of interstitial I^- with the substantially increased N_{ion} and lower E_a leads to an energy band structure opposite to what is needed for the narrowband photoresponse. This further supports our claim that the I^- accumulation in p-i-n type PPDs causes the p-type doping in the perovskite absorber and bends the band at the i-n interface, thereby leading to the narrowband spectral response.

4.2 | The OAED region affected by ion migration in the BMN-enabled narrowband PPDs

In the OAED region, if the energy band is not flat but is slanted as shown in Figure 2A, that is, there still exists a charge-separated electric field, there will be a nonzero photoresponse to short-wavelength photons. In previous works, trap states were generally introduced into the active layer, especially at the p-i interface to suppress the photoresponse in the short-wavelength region.[10,13,60]

Given that ion migration and subsequent narrowband photoresponse have been demonstrated above, we envisage that the ion migration could also lead to extension of OAED region near the light incident surface.

To simulate the dependence of EQE on the ion-migration governed OAED layer, we constructed a model with a simplified device structure of p-n junction consisting of a thick p-type active layer (perovskite) and a thin n-type layer (n-PCBM) due to the original p-type feature of our perovskite (Figure S13) and the dominant migration species of I^- (TID results). When the p-n junction is illuminated from the thick p-type layer, the EQE of the device contributed by the minority carrier currents (j_n and j_p) and the generation current (j_{gen}) can be expressed by[61]:

$$\text{EQE} = \frac{-j_n - j_p - j_{\text{gen}}}{qb_s} \tag{8}$$

where b_s is the spectral photon flux density.

$$j_{\text{gen}} = -qb_s(1-R)e^{-\alpha\left(x_p-\omega_p\right)}\left\{1-e^{-\alpha\left(\omega_p+\omega_n\right)}\right\} \tag{9}$$

where R is the reflectivity, α is the absorption coefficient, x_p is the thickness of the p-type active layer, ω_p is the depletion width in the p-type layer, and ω_n is the depletion width in the n-type layer.

In the thick p-n junction device considered here, both neutral regions are much thicker than the diffusion lengths, and thus the minority carrier currents can be approximated by:

$$j_n \approx -qb_s(1-R)e^{-\alpha\left(x_p-\omega_p\right)}\left(\frac{\alpha L_n}{1-\alpha L_n}\right) \tag{10}$$

$$j_p \approx -qb_s(1-R)e^{-\alpha\left(x_p+\omega_n\right)}\left(\frac{\alpha L_p}{1+\alpha L_p}\right) \tag{11}$$

where L_n and L_p are the diffusion lengths of electrons and holes, respectively. Using the electron and hole mobility derived from the space-charge-limited current (SCLC) method (Figures S16A,B) and the lifetime from the time-resolved photoluminescence (TRPL),[9] L_n and L_p were estimated to be 18.3 and 55.0 nm, respectively, both of which are much smaller than the perovskite layer thickness. Because the n-type layer is extremely thin (<30 nm) in comparison with the p-type layer (>2 μm), ω_n is approximately zero, and the depletion region falls entirely within the p-type layer. In contrast to the solar cell design, which usually has a thin, highly doped p-type layer and a thick, lightly doped n-type layer, a thick p-type active layer is necessary for our narrowband PPDs, as discussed above.

From Equations (10) and (11), the j_n and j_p show exponential dependence on x_p, and j_p can be assumed to be zero because x_p is large (>2 μm) in our PPDs. It is important to note that the neutral region in the p-type layer is regarded as the OAED region in our device, whose thickness is $x_{\text{OAED}} = x_p - \omega_p$. When x_{OAED} is small, j_n cannot be ignored. Therefore, j_{gen} and j_n can be rewritten as:

$$j_{\text{gen}} = -qb_s(1-R)\left(e^{-\alpha x_{\text{OAED}}} - e^{-\alpha x_p}\right) \tag{12}$$

$$j_n \approx -qb_s(1-R)e^{-\alpha x_{\text{OAED}}}\left(\frac{\alpha L_n}{1-\alpha L_n}\right) \tag{13}$$

The simulated EQEs contributed from j_{gen} and j_n with different x_{OAED} are shown separately in Figures 3C,D. Both j_{gen} and j_n at the short-wavelength (450 nm) show a dramatic drop with the increased x_{OAED} due to the low penetration power of the short-wavelength photons. On the contrary, the j_{gen} and j_n at the absorption edge (776 nm) show a relatively weak dependence on the x_{OAED} because the sub-bandgap photons can penetrate deeper into the p-type active layer. Thus, the spectral rejection ratio (SRR) can be effectively enhanced by increasing the x_{OAED}.

We measured EQE spectra of MAPbI_3 PPDs with various thicknesses of perovskites (Figures S17A–C) at 0 V bias before (Figure S17D) and after (Figure S17E) illumination. All devices exhibited broadband response before illumination but switched to narrowband response at the absorption edge after being illuminated for 4 min. Based on the simulation results above, we attribute this switching to the formation of the OAED region by the enhanced ion migration under illumination. Furthermore, the SRR increased with increasing perovskite layer thickness from 1.9 to 23.5 μm after illumination (Figure S17E), indicating that the E_{bi} is not completely screened by the E_{ion} in the OAED region under 4 min illumination. We further performed the finite-difference time-domain (FDTD) simulation to understand the optical field distribution in the PPDs containing a 25 μm thick perovskite layer. As shown in Figure S18, the observed penetration depth of light in the perovskite layer follows the Beer–Lambert law. The photons at wavelengths shorter than 700 nm can be mostly absorbed when arriving at the ~0.8 μm depth from the bottom of the perovskite layer. However, the photons at wavelengths around ~900 nm can penetrate much deeper to even throughout the whole 25 μm thick perovskite film. Therefore, the thickness of the perovskite layer has a significant impact on light absorption and carrier transport. We attributed the remaining photo-response in the short-wavelength region to the increased nominal diffusion length of carriers caused by the photon recycling effect in the perovskite film[34,62] and the imperfectly flat energy band in the OAED region. To further quench the photoexcited carriers in the short-wavelength region, an even thicker perovskite layer or enhanced ion migration effect should be considered, for example, by extending the film deposition time (Figures 1E,H), adding excess ions,[36] or introducing other external stimuli as we mentioned in Section 5.

To further probe the effect of ion migration on the OAED region, we conducted device simulations with the solar cell capacitance simulator (SCAPS) based on the ion-migration coupled drift-diffusion model (Figures 3E–G and Figures S19–S21). The model parameters of the p-NiO$_x$, MAPbI$_3$, and n-PCBM layers were obtained from the literature and summarized in Table S2. The effect of acceptor density (N_a) variation due to I$^-$ migration on the photoresponse of p-i-n-type PPDs was investigated. N_a(NiO$_x$) and N_a(PCBM) represent concentrations of the ions accumulated on the interfaces of perovskite. We considered three cases for the density profile N_a in the perovskite layer: (1) uniform (Figures S19A,B), (2) linearly increasing (Figures 3E,F), and (3) exponentially increasing (Figures S19C,D) distribution from the p-NiO$_x$ side to the n-PCBM side. Interestingly, the energy band and corresponding simulated EQE spectra of the MAPbI$_3$ PPDs present similar trends for all the three density distributions N_a. To simplify the demonstration, we set the density profile N_a in perovskite to increase linearly from the p-NiO$_x$ side (N_a(NiO$_x$) = 0) to the n-PCBM side (N_a(PCBM)) as in the aforementioned case (2). As shown in Figure 3E, with increasing N_a, the energy band close to the p-NiO$_x$ side becomes flat, while it drops significantly near the n-PCBM side. This ion migration-induced energy band change is exactly what we envisioned in Figures 2A,D. The corresponding electric field distribution of the perovskite layer is shown in Figure S20A, which is clearly stronger near the n-PCBM side but gradually decreases and becomes negligible near the p-NiO$_x$ side in the p-i-n type PPD. These simulation results verify the effect of ion migration on the OAED region and are consistent with the KPFM results (Figures 2C,F). Because of this energy band change, the EQE changes from broadband to narrowband (Figure 3F and Figure S20B).

The ion migration can be accelerated under illumination, which explains why the photodetector shows a narrowband response after illumination. To more clearly expose the narrowband photoresponse enhanced by ion migration, we present the simulated data in Figure 3F to plot the N_a-dependent SRR, which is defined as the ratio between the peak EQE (λ_{776}) and the adjacent EQE (λ_{450}) outside the target spectral range. As shown in Figure 3G, the SRR consistently increases with the N_a(PCBM) increasing from 10^{13} to 10^{15} cm^{-3}, directly proving the enhanced narrowband detection. For direct comparison, Figure 3H shows the experimental EQE spectra under persistent illumination. The coincidence between the experimental and simulation results is evident, although there are minor deviations in the magnitude of photoresponse in the short-wavelength region, mainly due to the default absorption coefficient settings in SCAPS. In addition, the simulated SRR in Figure S21B increases with the thickness of the perovskite layer which is again in agreement with the above-presented experimental result in Figure S17E.

Based on the comprehensive analysis of the experimental and simulation results, we can confidently conclude that the devices' photoresponse can be primarily governed by the ion migration and accumulation of negatively charged ions (interstitial I$^-$) at the perovskite/PCBM interface and the resulting energy band changes in the perovskite device. By skillfully manipulating ion migration, one can effectively regulate the OAED layer in the perovskite near the p-NiO$_x$ side and induce a down-bending band near the n-PCBM side. This effective control over the band modulation via ion migration allows us to influence the spatial distribution of charge carriers, ultimately enabling the manipulation of the photoresponse in the short-wavelength and long-wavelength regions.

5 | ACTIVE MANIPULATION OF BMN-ENABLED NARROWBAND PHOTODETECTION

As the ion migration dynamic in perovskites can be purposely manipulated via various external stimuli, we embarked on probing the impact of illumination, temperature, and external bias on the photoresponse of the devices and the feasibility of our proposed BMN mechanism for narrowband PPDs.

5.1 | Illumination

Light irradiation intensifies ion migration by reducing the ion migration barrier in halide perovskites.[21,63–67] As illustrated in Figures 4A,B, ion migration is driven by the inherent E_{bi} in the dark. Under light irradiation, it is E_{net} that drives the migrating ions to reach a new equilibrium. Regardless of the treatment order, the narrowband photoresponse was enhanced after illumination under

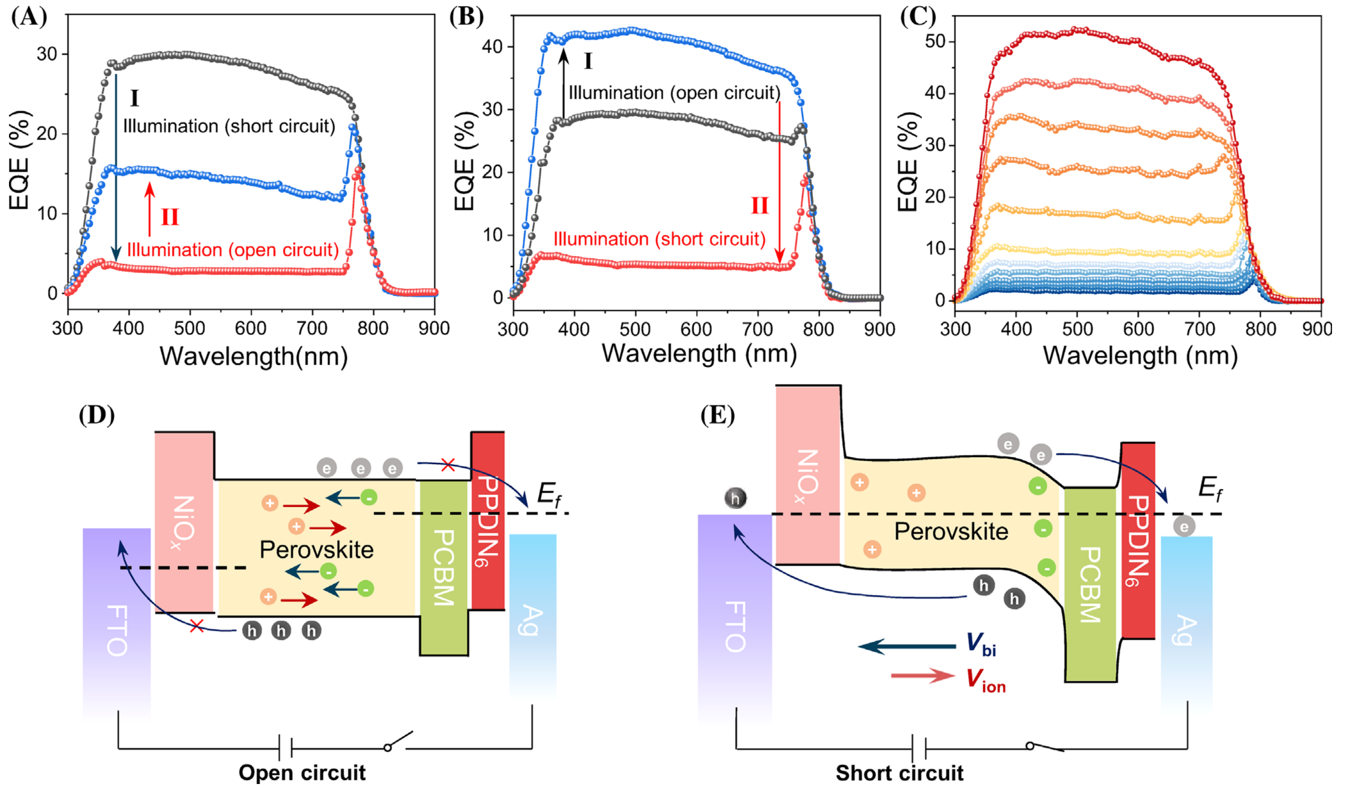

FIGURE 4 The effects of illumination, circuit conditions, and temperature on the EQE response of p-i-n type self-filtering narrowband perovskite photodetectors. (A,B) The EQE spectra of $MAPbI_3$ photodetector after illumination at short-circuit and then open-circuit (A), after illumination treatment at open-circuit and then short-circuit (B). (C) The EQE spectra of $MAPbI_3$ photodetector at different temperatures from 200 to 390 K. (D,E) Schematic showing the charge separation/collection of p-i-n type photodetectors under illumination at open-circuit (D) and short-circuit (E).

short-circuit conditions (see I in Figure 4A and II in Figure 4B). However, illumination under open-circuit conditions (see II in Figure 4A and I in Figure 4B) weakens the narrowband photoresponse increasing the EQE in the entire wavelength range. Under the open-circuit condition, the photoexcited electrons and holes cannot be efficiently extracted from the device, leading to their accumulation at the interfaces. These accumulated carriers will generate a field that offsets the field induced by the band alignment, resulting in a flat band under quasi-equilibrium conditions as shown in Figure 4D. In this case, the accumulated ions at the interfaces will then diffuse back into the perovskite, reducing the OAED region and increasing EQE across the entire spectral range. This behavior resembles the "light-soaking" effect[24,68,69] observed in perovskite-based solar cells. Under the short-circuit conditions, electrons and holes are efficiently extracted due to the presence of E_{bi} in the device (Figure 4E). With the lowered E_a under illumination, ions can easily migrate and accumulate at the interfaces, leading to an expanded OAED region and enhanced narrowband photoresponse.

5.2 | Temperature

Temperature plays a crucial role in affecting both electrical and ionic conductivity. Figure 4C shows the temperature-dependent EQE spectra of PPDs. As the temperature increases from 200 to 390 K, the EQE response of the $MAPbI_3$ PPD increases and the photoresponse converts from narrowband to broadband accordingly. This behavior can be attributed to the enhanced conductivity and reduced band bending with increased temperatures. When the temperature goes up, the ion distribution becomes more homogenized, causing fewer ions to pile up in the interfacial regions and suppressing the photogenerated carrier loss. Additionally, at higher temperatures, a larger number of thermally excited electrons move from the valence band to the conduction band, weakening the doping effect caused by ion accumulation. The higher diffusion coefficient also helps the ions diffuse back to the perovskite bulk rapidly, which can reduce the trap states and improve the carrier collection. We suspect the enhanced conductivity also plays a role in reducing the OAED region and weakening the down-band bending, thus broadening and largely enhancing the overall photoresponse of PPDs. Moreover, we observed a blue shift in the photoresponse edge (Figure 4C), which is consistent with the changes in the transmittance spectra and PL spectra (Figure S22). This shift can be explained by the broader bandgap caused by the perovskite lattice relaxation and the decreased overlap between the I^- and Pb^{2+} antibonding orbitals.[70–72]

Next, we conducted cyclic voltammetry on the PPDs at two different temperatures (300 and 360 K) in the dark (Figure S23). During the positive scan from 0 to 2.1 V at 300 K, the dark current of the device remains negligible until the applied bias surpasses V_{oc} (~1.6 V) with a large spike (Figure S23A). The current spike can be attributed to the fast diffusion of the accumulated ions from the interface back to the bulk perovskite due to the large concentration gradient when the external bias shields the E_{bi}. During the subsequent scan, the concentration gradient of ions decreases, resulting in reduced current and negative differential resistance.[73] However, no current spike was observed during the negative scan probably due to the much smaller concentration gradient. Restarting the measurement cycle can induce the current spike again due to the ion redistribution at the low applied bias, which could occur in seconds.[45] When the temperature was elevated to 360 K, the situation was quite different than we expected. The most significant change is that the current spike becomes obscure or even absent (Figure S23B). Conceivably, at higher temperatures, although ion migration is promoted to accumulate ions at the interface, faster ion diffusion to bulk perovskite appears to play a more dominant role in causing the absence of the spike.

5.3 | External bias

In our PPDs, ion migration is driven by the E_{bi}, and a balance between the ion accumulation at the interfaces and diffusion back to the bulk can be achieved at equilibrium. External bias (V_{app}) disrupts this balance by altering the devices' band structure and affecting ion distribution. The interplay between the E_{bi}, E_{ion}, V_{app}, and pretest conditions determines the kinetics of ion migration in the

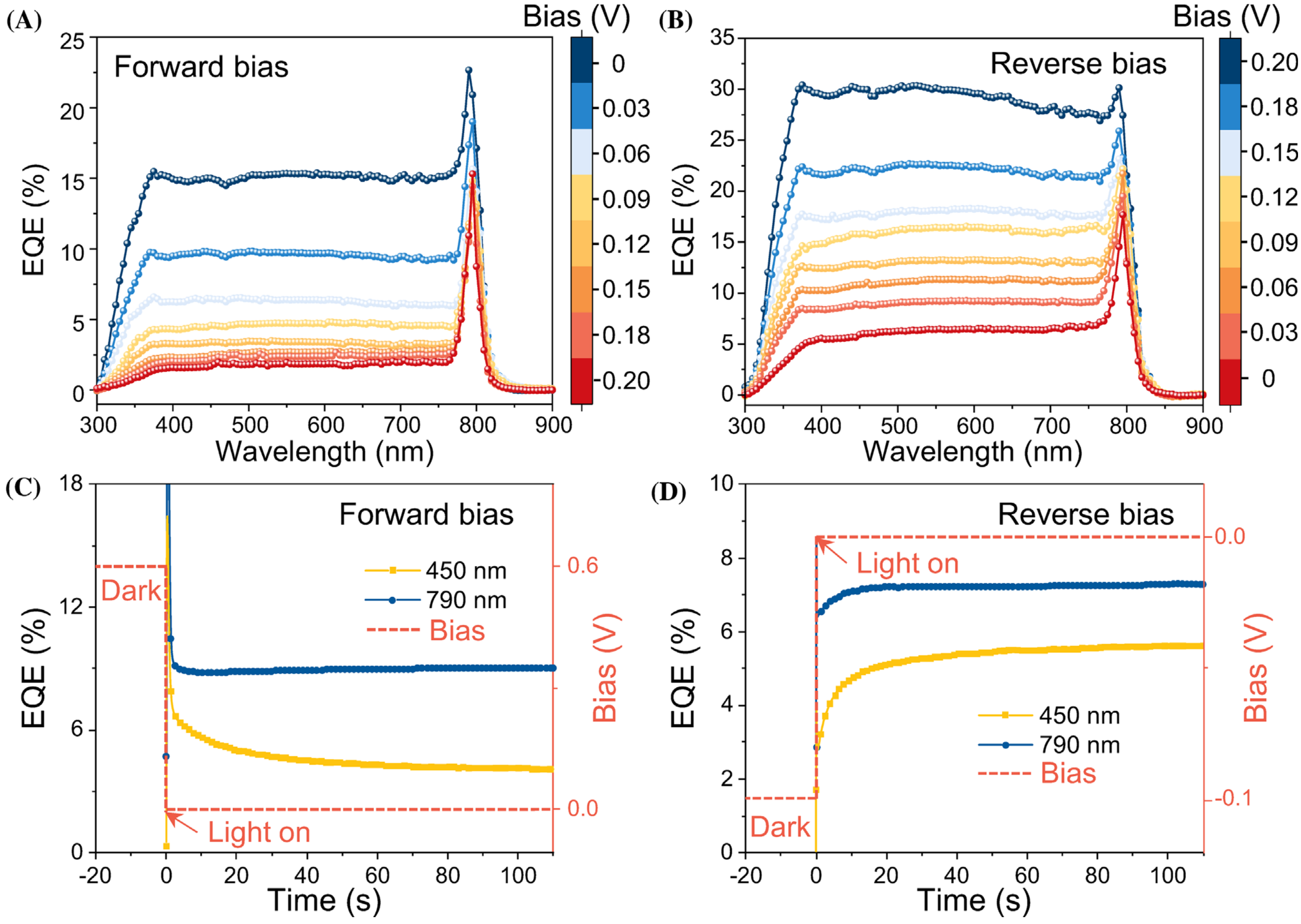

FIGURE 5 The dependence of EQE spectra on the external bias. (A,B) Bias-dependent EQE spectra for p-i-n type device under the forward bias (A), and reverse bias (B). (C,D) EQE spectra at 450 and 790 nm for a p-i-n type device after removing the forward bias (C) and reverse bias (D) for 20 s. The devices were provided with illumination when the bias was removed at $t = 0$ s.

PPDs. To directly observe the ion migration in perovskite under external bias, we conducted confocal photoluminescence microscopy on a lateral $MAPbBr_3$ perovskite device (Au^+/perovskite/Au^-) as shown in Video S1 and Figure S24. Bright areas in the images represent photoluminescence emission from the $MAPbBr_3$ perovskite films. Under a continuous positive external bias, we observed clear luminescence quenching in the perovskite near the Au^- side due to the migration of Br^- ions toward the Au^+ side (Figures S24A–D). However, when applying a negative bias, Br^- ions move back to the Au^- side, restoring the distribution of luminescence (Figures S24E,F). We note that the overall photoluminescence decreased with time. We attribute this to the defect accumulation and altered stoichiometry of the perovskite layer under the high bias.[74,75]

The bias-dependent EQE spectra of 10 μm-thick $MAPbI_3$ PPDs show that after illumination for 4 (Figure 5A) and 10 min (Figure 5B), the device at zero bias shows the expected narrow peak. External V_{app} redistributes ions until a new equilibrium is reached. As the forward bias increases, the EQE in the short-wavelength region decreases significantly due to the enlarged OAED layer, while the EQE in the absorption edge remains nearly unchanged, resulting in an enhanced narrowband photoresponse and SRR (Figure 5A). In contrast, for the device under reverse bias, the OAED layer in the perovskite narrows, and the E_{bi} plays a decisive role. Consequently, charges generated by short-wavelength light also contribute to the photocurrent, leading to a reduced SRR and significantly enhanced broadband photoresponse (Figure 5B).

We also conducted poling experiments by applying forward or reverse bias for 20 s, and then recording the EQE time profiles after bias removal. As illustrated in Figure 5C, after removing the forward bias (0.6 V) poling, the EQE values gradually decrease at the short-wavelength (450 nm) and barely change at the long-wavelength (776 nm). This is attributed to the counterbalanced E_{ion} gradually recovering to balance the E_{bi}, along with the ion migration and accumulation at the interfaces. On the other hand, after releasing the reverse bias (0.1 V) poling, the EQE values gradually increase at the short-wavelength (450 nm) and barely change at the long-wavelength (776 nm) as depicted in Figure 5D. This is because the migrated species begin to diffuse back into the perovskite bulk concurrent with the weakened band bending.

6 | CONCLUSIONS

In conclusion, we demonstrate an external-stimuli-controlled band modulation narrowing strategy to achieve self-filtering narrowband photoresponse by deliberately manipulating ion migration in the active materials. Through the studies using the SCAPS simulation and KPFM results, we have identified two crucial mechanisms for narrowband photodetection: the OAED layer with a flat band in the perovskite layer close to the p-NiO_x side and the down-bending energy band near the n-PCBM side. Our TID study showed the critical role of anion accumulation at the perovskite/PCBM interface in this mechanism. By deliberately manipulating external stimuli like bias, illumination, and temperature, we have solidified the feasibility and applicability of our proposed BMN mechanism. This mechanism provides a new in situ band modulation approach for perovskite-based devices, and is expected to play a significant role in the development and application of new functional devices.[76–78] Our work not only introduces an efficient and controllable approach to narrowband photodetection, but also significantly advances our understanding of the ion migration process in perovskite. Last but not the least, the narrowband photodetection scheme has been successfully demonstrated in exemplary organic–inorganic and all-inorganic perovskite-based narrowband photodetectors, and it holds high potential for extension to photodetectors based on other active materials exhibiting ion migration characteristics.

7 | EXPERIMENTAL SECTION

7.1 | Materials

The precursors used in this study include PbI_2 (98%, Sinopharm), $PbBr_2$ (>98%, Sigma-Aldrich), $PbCl_2$ (99%, TCI), MAI (98%, GreatCell Solar), MABr (98%, GreatCell Solar), MACl (98%, GreatCell Solar). *N*,*N*-dimethylformamide (DMF, 99%) and dimethyl sulfoxide (DMSO, 99%) reagents were purchased from Aladdin. Chlorobenzene (CB, extra dry, 99.9%) was obtained from Sigma-Aldrich. 2,2,2-Trifluoroethanol (TFE, extra pure, 99.8%) was supplied by Acros. PCBM was purchased from Xi'an Polymer Light Technology. Amino-functionalized perylene diimide polymer (PPDIN6) was synthesized using the methods reported previously.[35] All the chemicals were directly used without further purification. Patterned FTO glass substrates were obtained from Advanced ElectionTechnology Co., Ltd (China).

7.2 | Device fabrication

The prepatterned FTO glass was cleaned with detergent, distilled water, isopropanol, and anhydrous ethanol successively. After 5 min of oxygen plasma, acetonitrile solution of nickel (II) acetylacetonate (0.01 M) and diethanolamine (0.01 M) was sprayed on the FTO substrate using a homemade setup of the ultrasonic spray pyrolysis (USP) method.[35] The precursor solution was obtained by mixing PbX_2 and MAX (X = I, Br, Cl) into DMF/DMSO (1: 1.5, v/v) with stoichiometric proportion to gain the concentration of 0.8 mol L^{-1}. The perovskite films with different compositions were deposited using a homemade ALS method as previously reported.[29–31,79] After deposition, the perovskite films were annealed at 120°C for 10 min and then gradually cooled down to room temperature for 30 min. The fabricated perovskite films were then sequentially coated with PCBM solution (20 mg mL^{-1} in chlorobenzene) and PPDIN6 solution (0.5 mg mL^{-1} in trifluoroethanol) at 3000 r.p.m. for 30 s. Finally, the devices were finished by depositing 80 nm of Ag using thermal evaporation.

7.3 | Characterization

The morphology of the perovskite films and devices was measured by cold field-emission scanning electron microscopy (7800F, JEOL). The x-ray patterns of perovskite films were measured by Bruker D8 Advance with a Cu Kα radiation ($\lambda = 0.154056$ nm) as the x-ray source. The UV–vis absorption spectra and steady-state photoluminescence (excitation at 405 nm) spectra were performed on QSpec LTF-3000 (Biaoqi Optoelectronics, China). Scanning Kelvin probe force microscopy was performed on perovskite cross-sectional samples under open-circuit conditions in ambient conditions using a Bruker Dimension Icon using PeakForce Mode. The platinum-iridium-coated SCM-PIT-V2 probe was applied to measure the CPD values. The distances between the probe and the samples were all set to 100 nm. The Confocal PL spectra of $MAPbBr_3$ perovskite films were measured by a Nikon A1R confocal microscope at an excitation wavelength of 405 nm. The bias-dependent confocal movie was obtained by merging the time-lapse imaging. External quantum efficiencies were measured by the Zolix IPCE measurement system (Zolix, SCS10-150A-DSSC-CB07) with a calibrated silicon cell to measure the incident monochromatic light intensity. For the temperature-dependent characterization, the sample was mounted in a liquid nitrogen cryostat (Oxford Instruments, OptistatDN) to control the ambient temperature. The noise current spectral was measured by an FS-Pro™ semiconductor parameter analyzer (PRIMARIUS). The current density-voltage characteristics of the PPDs were obtained using a Keithley 2400 source-measure unit. The optical part of the LDR measurement was provided by a supercontinuum source (OYSL SC-Pro) which could produce 430–2000 nm illumination. The electrochemical impedance spectroscopy was measured by an electrochemical workstation from Zahner Company. The DLTS measurement was supported by the Phystech FT-1230 HERA-DLTS system in the dark and under the illumination of a 10-mW red laser (635 nm wavelength). The modified Boonton 7200 capacitance meter was used to measure the dynamic capacitance from 170 to 380 K at 2 K heating intervals. The pulse mode was set as electrical (pulse voltage) with a forward bias of 1 V, a pulse voltage of 0 V, a pulse width of 20 s, and a period width of 200 ms, respectively.

ACKNOWLEDGMENTS

The authors gratefully acknowledge the support of the National Natural Science Foundation of China (52202182, 22261160370, U2001217, 22275180, and 21972006), Shenzhen Peacock plan (KQTD2016053015544057), and Shenzhen Innovation Fund (JCYJ20220818101018038). Sean Reinecke and Makhsud I. Saidaminov are grateful to the Natural Sciences and Engineering Research Council of Canada (RGPIN-2020-04239) for financial support. The authors are deeply grateful to Dr. Marc Burgelman at the University of Gent, Belgium, for providing the SCAPS-1D software freely available for academic use. The authors also acknowledge Jintao Fu and Xingzhan Wei for the help of noise spectrum measurement.

CONFLICT OF INTEREST STATEMENT

The authors declare no conflict of interest.

ORCID

Shihe Yang https://orcid.org/0000-0003-0714-6320

REFERENCES

1. Dandin M, Abshire P, Smela E. Optical filtering technologies for integrated fluorescence sensors. *Lab Chip*. 2007;7(8):955-977.
2. Higashi Y, Kim KS, Jeon HG, Ichikawa M. Enhancing spectral contrast in organic red-light photodetectors based on a light-absorbing and exciton-blocking layered system. *J Appl Phys*. 2010;108(3):034502.
3. Cao F, Chen J, Yu D, et al. Bionic detectors based on low-bandgap inorganic perovskite for selective NIR-I photon detection and imaging. *Adv Mater*. 2020;32(6):e1905362.
4. Li LL, Deng YH, et al. Self-filtered narrowband perovskite photodetectors with ultrafast and tuned spectral response. *Adv Opt Mater*. 2017;5(22):1700672.
5. Sobhani A, Knight MW, Wang Y, et al. Narrowband photodetection in the near-infrared with a plasmon-induced hot electron device. *Nat Commun*. 2013;4(1):1643.
6. Cicek E, McClintock R, Cho CY, Rahnema B, Razeghi M. $Al_xGa_{1-x}N$-based solar-blind ultraviolet photodetector based on lateral epitaxial overgrowth of AlN on Si substrate. *Appl Phys Lett*. 2013;103(18):181113.

7. Wang X, Liu K, Chen X, et al. Highly wavelength-selective enhancement of responsivity in Ag nanoparticle-modified ZnO UV photodetector. *ACS Appl Mat Interfaces*. 2017;9(6):5574-5579.
8. Fang YJ, Dong QF, Shao YC, Yuan YB, Huang JS. Highly narrowband perovskite single-crystal photodetectors enabled by surface-charge recombination. *Nat Photonics*. 2015;9(10):679-686.
9. Wang J, Xiao S, Qian W, et al. Self-driven perovskite narrowband photodetectors with tunable spectral responses. *Adv Mater*. 2021;33(3):e2005557.
10. Lin Q, Armin A, Burn PL, Meredith P. Filterless narrowband visible photodetectors. *Nat Photonics*. 2015;9(10):687-694.
11. Shen L, Zhang Y, Bai Y, Zheng X, Wang Q, Huang J. A filterless, visible-blind, narrow-band, and near-infrared photodetector with a gain. *Nanoscale*. 2016;8(26):12990-12997.
12. Park H, Dan Y, Seo K, et al. Filter-free image sensor pixels comprising silicon nanowires with selective color absorption. *Nano Lett*. 2014;14(4):1804-1809.
13. Li J, Wang J, Ma J, et al. Self-trapped state enabled filterless narrowband photodetections in 2D layered perovskite single crystals. *Nat Commun*. 2019;10(1):806.
14. Liu GY, Wu Y, et al. Halide ion migration in lead-free all-inorganic cesium tin perovskites. *Appl Phys Lett*. 2021;119(3):031902.
15. Xiao Z, Yuan Y, Shao Y, et al. Giant switchable photovoltaic effect in organometal trihalide perovskite devices. *Nat Mater*. 2015;14(2):193-198.
16. Chen QL, Zhang Y, et al. Switchable perovskite photovoltaic sensors for bioinspired adaptive machine vision. *Adv Intell Syst Comput*. 2020;2(9):2000122.
17. deQuilettes DW, Zhang W, Burlakov VM, et al. Photo-induced halide redistribution in organic-inorganic perovskite films. *Nat Commun*. 2016;7(1):11683.
18. Chen YCA, Zhou WC, et al. In situ management of ions migration to control hysteresis effect for planar heterojunction perovskite solar cells. *Adv Funct Mater*. 2022;32(1):2108417.
19. Zhang T, Chen HN, et al. Understanding the relationship between ion migration and the anomalous hysteresis in high-efficiency perovskite solar cells: a fresh perspective from halide substitution. *Nano Energy*. 2016;26:620-630.
20. Liu J, Hu MY, et al. Correlations between electrochemical ion migration and anomalous device behaviors in perovskite solar cells. *ACS Energy Lett*. 2021;6(3):1003-1014.
21. Zhao Y, Zhou W, Han Z, Yu D, Zhao Q. Effects of ion migration and improvement strategies for the operational stability of perovskite solar cells. *Phys Chem Chem Phys*. 2021;23(1):94-106.
22. Zhu W, Wang S, Zhang X, Wang A, Wu C, Hao F. Ion migration in organic-inorganic hybrid perovskite solar cells: current understanding and perspectives. *Small*. 2022;18(15):e2105783.
23. Li B, Lin M, Kan C, et al. Revealing the correlation of light soaking effect with ion migration in perovskite solar cells. *Sol RRL*. 2022;6(7):2200050.
24. Zhao C, Chen B, Qiao X, Luan L, Lu K, Hu B. Revealing underlying processes involved in light soaking effects and hysteresis phenomena in perovskite solar cells. *Adv Energy Mater*. 2015;5(14):1500279.
25. Yen MC, Lee CJ, Liu KH, et al. All-inorganic perovskite quantum dot light-emitting memories. *Nat Commun*. 2021;12(1):4460.
26. Eames C, Frost JM, Barnes PRF, O'Regan BC, Walsh A, Islam MS. Ionic transport in hybrid lead iodide perovskite solar cells. *Nat Commun*. 2015;6(1):7497.
27. Tress W, Marinova N, Moehl T, Zakeeruddin SM, Nazeeruddin MK, Grätzel M. Understanding the rate-dependent J-V hysteresis, slow time component, and aging in $CH_3NH_3PbI_3$ perovskite solar cells: the role of a compensated electric field. *Energ Environ Sci*. 2015;8(3):995-1004.
28. Li C, Tscheuschner S, Paulus F, et al. Iodine migration and its effect on hysteresis in perovskite solar cells. *Adv Mater*. 2016;28(12):2446-2454.
29. Xu X, Qian W, Wang J, et al. Sequential growth of 2D/3D double-layer perovskite films with superior x-ray detection performance. *Adv Sci*. 2021;8(21):e2102730.
30. Qian W, Xu XW, et al. An aerosol-liquid-solid process for the general synthesis of halide perovskite thick films for direct-conversion x-ray detectors. *Matter*. 2021;4(3):942-954.
31. Wang J, Xu XW, et al. Self-driven perovskite dual-band photodetectors enabled by a charge separation reversion mechanism. *Adv Opt Mater*. 2021;9(17):2100517.
32. Liu Y, Yang Z, Cui D, et al. Two-inch-sized perovskite $CH_3NH_3PbX_3$ ($X = Cl, Br, I$) crystals: growth and characterization. *Adv Mater*. 2015;27(35):5176-5183.
33. Kitazawa N, Watanabe Y, Nakamura Y. Optical properties of $CH_3NH_3PbX_3$ ($X =$ halogen) and their mixed-halide crystals. *J Mater Sci*. 2002;37(17):3585-3587.
34. Gan ZX, Wen XM, et al. The dominant energy transport pathway in halide perovskites: photon recycling or carrier diffusion? *Adv Energy Mater*. 2019;9(20):1900185.
35. Meng X, Ho CHY, Xiao S, et al. Molecular design enabled reduction of interface trap density affords highly efficient and stable perovskite solar cells with over 83% fill factor. *Nano Energy*. 2018;52:300-306.
36. Yu SS, Li Y, et al. Ion migration as a new paradigm to boost self-driven perovskite narrowband photodetectors. *Adv Opt Mater*. 2023;11(16):2300302.
37. Almora O, Zarazua I, Mas-Marza E, Mora-Sero I, Bisquert J, Garcia-Belmonte G. Capacitive dark currents, hysteresis, and electrode polarization in lead halide perovskite solar cells. *J Phys Chem Lett*. 2015;6(9):1645-1652.
38. Luo DY, Zou TY, et al. Low-dimensional contact layers for enhanced perovskite photodiodes. *Adv Funct Mater*. 2020;30(24):2001692.
39. Byeon J, Kim J, Kim JY, et al. Charge transport layer-dependent electronic band bending in perovskite solar cells and its correlation to light-induced device degradation. *ACS Energy Lett*. 2020;5(8):2580-2589.
40. Nandal V, Nair PR. Predictive modeling of ion migration induced degradation in perovskite solar cells. *ACS Nano*. 2017;11(11):11505-11512.
41. Jacobs DA, Shen H, Pfeffer F, et al. The two faces of capacitance: new interpretations for electrical impedance measurements of perovskite solar cells and their relation to hysteresis. *J Appl Phys*. 2018;124(22):225702.
42. Yang Z, Dou JJ, Wang MQ. Interface engineering in n-i-p metal halide perovskite solar cells. *Sol RRL*. 2018;2(12):1800177.

43. Kim HS, Park NG. Parameters affecting I-V hysteresis of $CH_3NH_3PbI_3$ perovskite solar cells: effects of perovskite crystal size and mesoporous TiO_2 layer. *J Phys Chem Lett*. 2014;5(17):2927-2934.
44. McGovern L, Futscher MH, Muscarella LA, Ehrler B. Understanding the stability of $MAPbBr_3$ versus $MAPbI_3$: suppression of methylammonium migration and reduction of halide migration. *J Phys Chem Lett*. 2020;11(17):7127-7132.
45. Futscher MH, Lee JM, McGovern L, et al. Quantification of ion migration in $CH_3NH_3PbI_3$ perovskite solar cells by transient capacitance measurements. *Mater Horizons*. 2019;6(7):1497-1503.
46. Reichert S, Flemming J, An Q, Vaynzof Y, Pietschmann JF, Deibel C. Ionic-defect distribution revealed by improved evaluation of deep-level transient spectroscopy on perovskite solar cells. *Phys Rev Appl*. 2020;13(3):034018.
47. Futscher MH, Gangishetty MK, Congreve DN, Ehrler B. Quantifying mobile ions and electronic defects in perovskite-based devices with temperature-dependent capacitance measurements: frequency vs time domain. *J Chem Phys*. 2020;152(4):044202.
48. Bai Y, Chen H, Xiao S, et al. Effects of a molecular monolayer modification of NiO nanocrystal layer surfaces on perovskite crystallization and interface contact toward faster hole extraction and higher photovoltaic performance. *Adv Funct Mater*. 2016;26(17):2950-2958.
49. Xue Q, Bai Y, Liu M, et al. Dual interfacial modifications enable high performance semitransparent perovskite solar cells with large open circuit voltage and fill factor. *Adv Energy Mater*. 2017;7(9):1602333.
50. Xu J, Buin A, Ip AH, et al. Perovskite-fullerene hybrid materials suppress hysteresis in planar diodes. *Nat Commun*. 2015;6(1):7081.
51. Zheng X, Chen B, Dai J, et al. Defect passivation in hybrid perovskite solar cells using quaternary ammonium halide anions and cations. *Nat Energy*. 2017;2:17102.
52. McGovern L, Koschany I, Grimaldi G, Muscarella LA, Ehrler B. Grain size influences activation energy and migration pathways in $MAPbBr_3$ perovskite solar cells. *J Phys Chem Lett*. 2021;12(9):2423-2428.
53. Egger DA, Kronik L, Rappe AM. Theory of hydrogen migration in organic–inorganic halide perovskites. *Angew Chem Int Ed*. 2015;54(42):12437-12441.
54. Azpiroz JM, Mosconi E, Bisquert J, De Angelis F. Defect migration in methylammonium lead iodide and its role in perovskite solar cell operation. *Energ Environ Sci*. 2015;8(7):2118-2127.
55. Jong UG, Yu CJ, Ri GC, et al. Influence of water intercalation and hydration on chemical decomposition and ion transport in methylammonium lead halide perovskites. *J Mater Chem A*. 2018;6(3):1067-1074.
56. Li C, Guerrero A, Huettner S, Bisquert J. Unravelling the role of vacancies in lead halide perovskite through electrical switching of photoluminescence. *Nat Commun*. 2018;9(1):5113.
57. Senocrate A, Moudrakovski I, Kim GY, et al. The nature of ion conduction in methylammonium lead iodide: a multimethod approach. *Angew Chem Int Ed*. 2017;56(27):7755-7759.
58. Senocrate A, Moudrakovski I, Acartürk T, et al. Slow $CH_3NH_3{}^+$ diffusion in $CH_3NH_3PbI_3$ under light measured by solid-state NMR and tracer diffusion. *J Phys Chem C*. 2018;122(38):21803-21806.
59. McGovern L, Grimaldi G, Futscher MH, et al. Reduced barrier for ion migration in mixed-halide perovskites. *ACS Appl Energy Mater*. 2021;4(12):13431-13437.
60. Miao JL, Zhang FJ. Recent progress on highly sensitive perovskite photodetectors. *J Mater Chem C*. 2019;7(7):1741-1791.
61. Nelson J. *The Physics of Solar Cells*. London: Imperial College Press; 2003. pp. 166-171.
62. Pazos-Outon LM, Szumilo M, et al. Photon recycling in lead iodide perovskite solar cells. *Science*. 2016;351(6280):1430-1433.
63. Li N, Jia Y, Guo Y, Zhao N. Ion migration in perovskite light-emitting diodes: mechanism, characterizations, and material and device engineering. *Adv Mater*. 2022;34(19):e2108102.
64. Zhang T, Hu C, Yang S. Ion migration: a “double-edged sword” for halide-perovskite-based electronic devices. *Small Methods*. 2019;4(5):1900552.
65. Mao W, Hall CR, Bernardi S, et al. Light-induced reversal of ion segregation in mixed-halide perovskites. *Nat Mater*. 2021;20(1):55-61.
66. Ouyang Y, Jiang XX, et al. Light-soaking induced optical tuning in rare earth-doped all-inorganic perovskite. *Adv Funct Mater*. 2022;32(2):2107086.
67. Zhao Y, Zhou W, et al. Quantification of light-enhanced ionic transport in lead iodide perovskite thin films and its solar cell applications. *Light Sci Appl*. 2017;6(5):e16243.
68. Yang C, Hu Z, Gao C, et al. Elimination of light-soaking effect in hysteresis-free perovskite solar cells by interfacial modification. *J Phys Chem C*. 2019;124(3):1851-1860.
69. Watts CL, Aspitarte L, Lin YH, et al. Light soaking in metal halide perovskites studied via steady-state microwave conductivity. *Commun Phys*. 2020;3(1):73.
70. Hoque MN, Islam N, et al. Ionic and optical properties of methylammonium lead iodide perovskite across the tetragonal-cubic structural phase transition. *ChemSusChem*. 2016;9(18):2692-2698.
71. Moot T, Patel JB, McAndrews G, et al. Temperature coefficients of perovskite photovoltaics for energy yield calculations. *ACS Energy Lett*. 2021;6(5):2038-2047.
72. Filip MR, Eperon GE, Snaith HJ, Giustino F. Steric engineering of metal-halide perovskites with tunable optical band gaps. *Nat Commun*. 2014;5(1):5757.
73. Ma H, Wang W, Xu H, et al. Interface state-induced negative differential resistance observed in hybrid perovskite resistive switching memory. *ACS Appl Mater Interfaces*. 2018;10(25):21755-21763.
74. Bai S, Da P, et al. Planar perovskite solar cells with long-term stability using ionic liquid additives. *Nature*. 2019;571(7764):245-250.
75. Pan D, Fu Y, Chen J, Czech KJ, Wright JC, Jin S. Visualization and studies of ion-diffusion kinetics in cesium lead bromide perovskite nanowires. *Nano Lett*. 2018;18(3):1807-1813.
76. Guo L, Sun H, Wang M, et al. A single-dot perovskite spectrometer. *Adv Mater*. 2022;34(33):2200221.
77. Xu X, Han Z, Zou Y, et al. Miniaturized multispectral detector derived from gradient response units on single $MAPbX_3$ microwire. *Adv Mater*. 2022;34(9):2108408.
78. Sun H, Tian W, Wang X, Deng K, Xiong J, Li L. In situ formed gradient bandgap-tunable perovskite for ultrahigh-speed color/spectrum-sensitive photodetectors via electron-donor control. *Adv Mater*. 2020;32(14):1908108.
79. Wang M, Gao W, Cao F, Li L. Ethylamine iodide additive enables solid-to-solid transformed highly oriented

perovskite for excellent photodetectors. *Adv Mater*. 2022;34(8):e2108569.

SUPPORTING INFORMATION

Additional supporting information can be found online in the Supporting Information section at the end of this article.

How to cite this article: Li Y, Yu S, Yang J, et al. Filterless narrowband photodetectors enabled by controllable band modulation through ion migration: The case of halide perovskites. *InfoMat*. 2024;6(1):e12506. doi:10.1002/inf2.12506